

Detection of Surface Brightness Fluctuations in Elliptical Galaxies imaged with the Advanced Camera for Surveys. B- and I-band measurements¹

Michele Cantiello^{2,3}, Gabriella Raimondo³, John P. Blakeslee², Enzo Brocato³, Massimo Capaccioli^{4,5}

ABSTRACT

Taking advantage of the exceptional capabilities of ACS on board of HST, we derive Surface Brightness Fluctuation (SBF) measurements in the B and I bands from images of six elliptical galaxies with $1500 \leq cz \leq 3500$. Given the low S/N ratio of the SBF signal in the blue band images, the reliability of the measurements is verified both with numerical simulations and experimental data tests.

This paper presents the first published B- and I-band SBF measurements for distant (≥ 20 Mpc) galaxies, essential for the comparisons of the models to observations of normal ellipticals. By comparing I-band data with our new Simple Stellar Population (SSP) models we find an excellent agreement and we confirm that I-band SBF magnitudes are mainly sensitive to the metallicity of the dominant stellar component in the galaxy, and are not strongly affected by the contribution of possible secondary stellar components. As a consequence I-band fluctuations magnitudes are ideal for distance studies. On the other hand, we show that standard SSP models do not reproduce the B-band SBF magnitudes of red ($(B - I)_0 \gtrsim 2.1$) galaxies in our sample. We explore the capability of two non-canonical models in properly reproducing the high sensitivity of B SBF to the presence of even small fractions of bright, hot stars (metal poor

¹Based on observations made with the NASA/ESA Hubble Space Telescope, which is operated by the Association of Universities for Research in Astronomy, Inc., under NASA contract NAS 5-26555. These observations are associated with programs #9427.

²Department of Physics and Astronomy, Washington State University, Pullman, WA 99164.

³INAF–Osservatorio Astronomico di Teramo, Via M. Maggini, I-64100 Teramo, Italy

⁴Dipartimento di Scienze Fisiche, Università Federico II di Napoli, Complesso Monte S. Angelo, via Cintia, 80126, Napoli, Italy

⁵INAF–Osservatorio Astronomico di Capodimonte, via Moiariello 16, 80131 Napoli, Italy

stars, hot evolved stars, etc.). The disagreement is solved both by taking into account hot (Post-AGB) stars in SSP models and/or by adopting Composite Stellar Population models. Finally, we suggest a limit value of the S/N for the B-band SBF signal required to carry out a detailed study of stellar population properties based on this technique.

Subject headings: galaxies: elliptical and lenticular, cD – galaxies: photometry – galaxies: evolution – galaxies: stellar component

1. Introduction

The first applications of the Surface Brightness Fluctuations (SBF) technique were mainly devoted to refine the method itself, and to gauge distances of elliptical galaxies and bulges of spirals up to ~ 20 Mpc (e.g., Tonry & Schneider 1988; Tonry et al. 1989, 1990; Tonry 1991; Jacoby et al. 1992). A deeper understanding of the SBF technique, together with technological improvements of telescopes, made it possible to extend the method to distances as far as ~ 100 Mpc (Jensen et al. 2001) with uncertainties typically lower than 10%, and to measure luminosity fluctuations for a wider family of astronomical objects ranging from Galactic and Magellanic Clouds globular clusters (Ajhar & Tonry 1994; González et al. 2004; Raimondo et al. 2005), to dwarf ellipticals (Jerjen et al. 1998, 2000; Mieske & Hilker 2003), in addition to the usual targets (elliptical galaxies and bulges spirals).

In their seminal paper Tonry & Schneider suggested that it was also possible to take advantage of SBF to analyze the metallicity and age of the stellar system in the galaxy. Such connection was revealed through the correlation between the SBF amplitudes and the integrated color of the galaxy. This behavior, effectively detected only after a substantial number of measurements was available (Tonry et al. 1990), on one hand showed that to obtain reliable SBF-based distances SBF versus integrated color relations must be used to “standardize” the SBF absolute magnitude. On the other hand, it also emphasized the possible use of the SBF as a tracer of stellar population properties.

The link between SBF and stellar populations is easily understood considering that, given the image of a galaxy, the SBF signal rises from the statistical fluctuation between adjacent regions, due to the finite number of stars per resolution element. In particular the SBF is defined as the spatial fluctuation of the galaxy surface brightness, normalized to the surface brightness itself. As demonstrated by Tonry & Schneider, by definition the SBF amplitude corresponds to the ratio of the second to the first moments of the luminosity function of the underlying stellar system. This means that, for a typical stellar population

of an early-type galaxy composed mainly by old and metal rich stars ($t \gtrsim 5$ Gyr, $[\text{Fe}/\text{H}] \gtrsim -0.3$), the SBF nearly corresponds to the average magnitude of the red giant branch (RGB) stars in the population. In this view – keeping in mind that stellar systems with different metallicities and ages have different RGBs, thus different SBF – the connection between SBF and stellar populations is clear.

In order to use SBF measurements to analyze the age and chemical composition of stellar systems, when individual stars cannot be resolved, there are two facts to be considered. First, on the observational side, in addition to the apparent SBF magnitude an estimation of the galaxy distance is needed so that the absolute SBF magnitude can be derived; otherwise, SBF color or SBF gradient data, which are distance-independent, are needed. Second, theoretical values for the absolute SBF magnitudes must be available.

The theoretical study of fluctuations amplitudes has been widely explored in the last decade, typically using Simple Stellar Population models (SSP). Since Tonry et al. (1990), many other authors (e.g., Buzzoni 1993; Worthey 1993b; Blakeslee et al. 2001; Liu et al. 2000; Cantiello et al. 2003; Mouhcine et al. 2005; Raimondo et al. 2005; Marín-Franch & Aparicio 2006) explored a wide range of metallicities ($0.0001 \lesssim Z \lesssim 0.05$), ages ($20 \text{ Myr} \lesssim t \lesssim 18 \text{ Gyr}$), in various wavelength intervals. These models showed a general agreement, though they are based on quite different input stellar physics. A general conclusion drawn from all models is that SBF magnitudes at shorter wavelengths intervals, e.g. in the B-band, show a stronger sensitivity to the chemical composition and age with respect to other bands, thus they must be preferred to address stellar population studies. This is particularly interesting in objects like elliptical galaxies, where dust pollution (which strongly affects bluer bands) is negligible or recognizable as irregular spots in the otherwise regular galaxy profile.

Up to now, the few examples on the use of SBF to probe the unresolved stellar content of galaxies have been based mainly on the comparison with models of the absolute fluctuation magnitudes \bar{M}_λ in a certain wavelength interval $[\lambda, \lambda + \Delta\lambda]$, thus relying on some assumption of the galaxy distance. There are fewer studies based on SBF color data, due to the general lack of multi-wavelength SBF data for the same galaxy. One recent application to galaxies is the work by Jensen et al. (2003) which couples ground-based I-band SBF with near-IR (F160W) HST data. Finally, only a few works presented SBF radial gradients within galaxies (Tonry 1991; Sodemann & Thomsen 1995; Tonry et al. 2001; Cantiello et al. 2005).

The aim of this paper is to present a set of B- and I-band SBF measurements for a selected sample of galaxies imaged with the ACS camera on board of HST. In Cantiello et al. (2005, C05 hereafter) we succeeded in revealing \bar{M}_I radial ($10 \lesssim r(\text{arcsec}) \lesssim 40$) gradients within 7 early-type galaxies. For six of these galaxies F435W (\sim Johnson B-band) images are also available. Taking advantage of the capabilities of the ACS camera, in this paper we

present the SBF analysis for the B images, whose SBF signal is expected to be substantially fainter than in the I-band images. To produce a homogeneous set of measurements for both bands, we repeat the SBF analysis also for I-band data adopting the same constraints (masks, regions for the SBF measurements, etc.) as for the B images.

The paper is organized as follows. Section 2 describes the selected sample of objects, the procedures adopted to derive the surface photometry, the photometry of point-like and extended sources, and the SBF magnitudes. In section 3 we introduce some tests performed to check the quality of our SBF measurements on B-band frames. The analysis of some observational properties of the galaxies sampled (plus two more objects whose data are taken from the literature), and the comparison of data with models are presented in section 4. We finish this paper with the conclusions, in section 5.

2. Data reduction and analysis

2.1. Observations

Five of the galaxies considered here are the same presented in C05 (NGC 1407, NGC 3258, NGC 3268, NGC 5322 and NGC 5557), while NGC 404 and NGC 1344 were excluded because no F435W images are available. The raw data are ACS F435W, and F814W exposures drawn from the HST archive. All data are taken with ACS in its Wide Field Channel mode. The observations are deep exposures associated with the proposal ID #9427, which was designed to investigate the Globular Cluster System for a sample of 13 giant ellipticals in the redshift regime $1500 \leq cz \leq 5000$. Among these galaxies we selected six objects less polluted by dust patches and with exposure times long enough to allow SBF measurements. Table 1 summarizes some properties of the galaxies sampled together with the exposure times in each filter.

As in C05, the image processing (including cosmic-ray rejection, alignment, and final image combination) is performed with the “Apsis” data reduction software (Blakeslee et al. 2003). The ACS photometric zero points and extinction ratios are from Sirianni et al. (2005, hereafter S05), along with a correction for Galactic absorption from Schlegel et al. (1998). Because of the small quantity of dust in normal elliptical galaxies, no internal extinction correction has been considered here. The dusty patches present in the case of NGC 4696 can be easily recognized in the B-band images and have been masked out. For this galaxy the percentage of the image area masked for dust is <2% of the whole ACS field of view (or < 8% the final area selected for SBF measurement).

To transform the ACS photometry to the standard UBVRI photometric system, we use

the equations from S05. For the B-, and I-band data the average difference between the ACS magnitudes and the ones obtained after applying the S05 equations does not exceed 0.03 mag. In C05 we presented some consistency checks of the (F435W, F814W)-to-(B,I) transformations, by comparing for each galaxy the transformed magnitudes and colors with available measurements taken in the standard photometric system. The results of the comparisons supported the reliability of S05 equations for the selected filters (see C05 for more details).

2.2. Data analysis

The procedure adopted to derive SBF measurements from the B-band frames is the same described in C05, with minor changes which will be discussed below together with a brief summary of the whole procedure.

2.2.1. Galaxy modeling and sky subtraction

Galaxy light profile modeling and subtraction, sky subtraction, and sources masking proceeded in an iterative way. Briefly, a provisional sky value for the whole image is assumed to be equal to the median pixel value in the corner with the lowest number of counts. After this sky value has been subtracted from the original image, we started an iterative procedure where: (i) the fit of the median galaxy profile is obtained using the IRAF/STSDAS task ELLIPSE; (ii) all the foreground stars, background galaxies, and the galaxy’s globular clusters (*external sources* hereafter) detected in the sky+galaxy subtracted frame are masked out; (iii) a new sky value is obtained by fitting a $r^{1/4}$ law to the surface brightness profile of the galaxy.

The procedure is then repeated, each time the ellipse fitting is performed using the updated mask of external sources, until convergence. As shown in C05, the uncertainty of assuming a $r^{1/4}$ profile instead of a $r^{1/n}$ or a Nuker profile, does not alter significantly the final value of integrated and SBF magnitudes, at least in the regions where the galaxy’s signal is higher than the background. The galaxy counts in the regions where the SBF color measurements were made are on average a factor ~ 7 (~ 17) higher than the sky level in the B (I) images.

2.2.2. Photometry of point-like and extended sources

Once the sky and the galaxy model were subtracted from the original image, we derived the photometry of the external sources. The construction of the photometric catalogue of point-like and extended sources is critical for the estimation of the Luminosity Function (LF). As is shown in C05, by fitting the LF of external sources (i.e. of globular clusters and background galaxies) we can infer, by extrapolation, its faint end, which must be determined to have reliable SBF measurements. This is due to the fact that the fluctuations measured from the sky+galaxy subtracted frame also include a contribution arising from the undetected external sources left in the image. A reliable LF model allows one to properly estimate and subtract such residual extra-fluctuation (usually indicated as P_r) from the total fluctuations signal, P_0 .

To obtain the photometry of external sources we used the software SExtractor (Bertin & Arnouts 1996), as it gives good photometry of both point-like and extended objects. It also gives as output a smoothed background map which is essential to remove the large scale residuals from the galaxy subtracted frame. Moreover, it accepts user specified weight images, and this is of great importance for our measurements, as, by specifying the error map, the photometric uncertainty can be estimated taking into account the contribution to the noise due to the subtracted galaxy. We have modified the SExtractor input weight images by adding to the RMS image the galaxy model times a constant factor ~ 0.5 for B-, and ~ 1 for I-band images. The constant factors have been chosen, after several checks, so that the surface brightness fluctuations are recognized as noise (Tonry et al. 1990), lower coefficient values would result in the detection and masking of fluctuations as external sources; on the contrary, higher values would result in many real external sources being undetected and therefore affect the SBF measurement.

We ran SExtractor on the residual images (i.e., galaxy+sky+large scale residuals subtracted images) independently for each band. The best parameters for source detection have been chosen by using numerical simulations. In particular, we have simulated images with known input LF, then the simulated images have been analyzed in the same way of real frames to study the LF of the sources detected. Finally the input LF have been compared with the ones derived from our standard analysis of the frame.

As an example of this procedure, in Figure 1 we show the derived best-fit of the LF of external sources obtained to determine the optimal *Detection Threshold* (DETECT_THRESH, $\sigma_{D.T.}$ hereafter) SExtractor parameter¹.

¹ We have used a fixed DETECT_MINAREA ~ 5 , corresponding to the PSF area of our ACS images.

In detail, we changed $\sigma_{D.T.}$ within the interval 0.5-50, obtaining different photometric catalogs, each one characterized by the number of sources detected in both frames, and by the average magnitude of the sources detected m^{fix} . Lowering the $\sigma_{D.T.}$ one has correspondingly (i) an increasing number of sources detected, (ii) a fainter average magnitude detected m^{fix} , and (iii) an increasing number of spurious detections. In the Figure 1 we plot with full dots the total observed number ($N_{detected}$) of detected sources brighter than m^{fix} versus m^{fix} for B (upper left panel), and I band (upper right panel). The solid line in these panels shows the input total number of sources (N_{input}). The lower panels show the residuals, i.e. : $\Delta N = |N_{detected} - N_{input}|$. We have chosen as final detection parameter $\sigma_{D.T.} = 1.3$ as for this value ΔN remains below 50 for both I-, and B-band frames, i.e., below $\sim 5\%$ of the total number of sources detected (for high number of detections).

The final photometric catalogs of external sources from B- and I-band images were matched using a radius $0.1''$. On average, the number of objects clearly detected in the I-band frame and undetected in the B-band one, e.g. red galaxies, is $\lesssim 30$. We have verified that including the photometry of these missing objects does not significantly alter the LF model and therefore the correction to the SBF signal for undetected sources is not significantly changed.

Once the catalogue of matched sources was constructed, we applied the aperture correction as in C05. That is, for point-like sources we derived the aperture correction by making a growth-curve analysis over few bright, well isolated point sources in the frame (Stetson 1990). The aperture correction was obtained by summing the contribution evaluated from the growth-curve analysis, with aperture diameters 6-20 pixels, and the contribution from 20 pixels to “infinite” diameter reported by S05. For extended sources, instead, we used the aperture correction following the prescriptions by Benítez et al. (2004).

A model LF was then derived from the final photometric catalogue by assuming the total number density to be the sum of a gaussian-shaped Globular Cluster LF (GCLF, Harris 1991):

$$n_{GC}(m) = \frac{N_{0,GC}}{\sqrt{2\pi\sigma^2}} e^{-\frac{(m-m_{\lambda,GC})^2}{2\sigma^2}} \quad (1)$$

and a power-law LF (Tyson 1988) for the background galaxies:

$$n_{gxy}(m) = N_{0,gxy} 10^{\gamma m} \quad (2)$$

The SExtractor detection S/N limit is $\sigma_{D.T.} \times \sqrt{DETECT_MINAREA}$. For this test we have used the images simulated according to prescriptions presented in section 3. This allowed us to compare the observed integrated luminosity function with the input one.

where $N_{0,GC}$ ($N_{0,gxy}$, Blakeslee & Tonry 1995) is the globular cluster (galaxy) surface density, and $m_{\lambda,GC}$ is the turnover magnitude of the GCLF at the galaxy distance. In expression (2) we used the γ values obtained by Benítez et al. (2004). For the GCLF we assumed the turnover magnitude and the width of the gaussian function from Harris (2001). To fit the total LF we used the software developed for the SBF distance survey; we refer the reader to Tonry et al. (1990) and Jacoby et al. (1992) for a detailed description of the procedure. Briefly: a distance modulus (μ_0) for the galaxy is adopted in order to derive a first estimation of $m_{\lambda,GC} = \mu_0 + M_{\lambda,GC}$, then an iterative fitting process is started with the number density of galaxies and GC, and the galaxy distance allowed to vary until the best values of $N_{0,GC}$, $N_{0,gxy}$ and $m_{\lambda,GC}$ are found via a maximum likelihood method.

Figure 2 exhibits the observed B- and I-band LF for the whole sample of galaxies, and their best fit curves. In this figure we report the LF over the entire area analyzed, although the SBF analysis is conducted independently in annuli (Tonry et al. 1990).

The source catalogue is then used to mask all sources brighter than a (radially dependent) completeness limit. The residual fluctuation amplitude due to the remaining undetected faint sources, P_r , is then evaluated as described in C05.

As shown in Table 2 I-band SBF magnitudes are not strongly affected by the P_r correction, which is typically a factor 20 smaller than the stellar fluctuations amplitude, P_f . The case of B-band SBF is quite different. In this case, the amplitude of the stellar SBF competes with the residual variance from undetected sources. For B-band measurements, in fact, we find an average $P_r \sim 0.22P_f$. However, even in the case of B-band data, the accuracy of photometric catalogue allowed to obtain a reliable LF model.

In order to estimate the uncertainty associated to P_r we have carried out several numerical experiments by using the tool described in forthcoming section 3. In particular, we have estimated P_r from simulations of ACS images having similar properties to our real images and compared it with the known input value. We obtained that a realistic estimation of the P_r uncertainty is $\sim 20\%$ the value of P_r . In addition we have also estimated that changes up to 50% of the original value in the LF fitting parameters (γ , $M_{\lambda,GC}$, etc.) affect the final P_r by less than 15%. In conclusion we adopt 20% of P_r as an estimate of its uncertainty.

2.2.3. SBF measurements

The SBF analysis executed for B-band frames is similar to the one described in C05, except for the fact that here we derive one single SBF value per galaxy (instead of different SBF measurements in several concentric annuli as in C05) since B-band images do not achieve

a sufficiently high S/N to make a detailed study of the fluctuation amplitude as a function of radius.

For sake of homogeneity we also re-analyzed I-band images by adopting the same annuli shape as from the B frames. The annulus was created using a mask that matches the ellipticity and position angle of a given region. All frames were analyzed in the same way. After subtracting the sky, the galaxy model, and the large scale residuals, we derived (i) the photometry of point-like and extended sources in the frame, masking (ii) all sources above a fixed S/N ratio (~ 3.0). Afterwards, the residual frame divided by the square root of the galaxy model was Fourier transformed (iii), and the azimuthal average of the power-spectrum $P(k)$ evaluated. Then we derived (iv) the constants P_0 and P_1 in the equation:

$$P(k) = P_0 \cdot E(k) + P_1, \quad (3)$$

adopting a robust linear least squares method (Press et al. 1992). In the latter equation $E(k)$ is the azimuthal average of the convolution between the PSF and the mask power spectra. The PSF used were the template PSF from the ACS IDT, constructed from bright standard star observations. Finally, the SBF amplitude in magnitude was obtained as:

$$\bar{m} = -2.5 \log(P_0 - P_r) + mag_{zero} - A_\lambda. \quad (4)$$

Here P_r is the residual variance due to unmasked sources in the frame, which has been estimated from the LF of the external sources detected in the frame (section 2.2.2, and C05). The constant mag_{zero} is the zeropoint magnitude from S05, while A_λ is the extinction correction.

To test the stability of these measurements, we performed several tests. As an example, we have chosen few well isolated point sources available in the frames, repeating the fitting operations for eq. (3) using these new objects as PSF references. The resulting SBF magnitudes agree with the previous measurements within uncertainties. The final P_0 , P_1 , P_r and P_f values are reported in Table 2, while the SBF magnitudes and $(B - I)_0$ color are reported in Table 3, together with other properties of the galaxies. The SBF error estimates includes: (i) the error in the determination of P_0 , (ii) a $\sim 5\%$ error from the PSF (C05), and (iii) the uncertainty of P_r , all summed in quadrature. As shown in C05, the effect on SBF arising from sky uncertainty is negligible.

The distance moduli reported in Table 3 are derived averaging the group distance moduli estimations of FP and IRAS velocity maps distribution (Table 6 data in C05). For NGC 5557, since no group distance is known, we adopted the weighted average distance estimations for

the galaxy itself. M32 distance is derived as weighted averages of group distances from the Ferrarese et al. (2000) database, excluding SBF based distances. NGC5128 distance comes from the recent Ferrarese et al. (2007), based on Cepheids variables.

3. Checks on SBF measurements reliability

As discussed in Jensen et al. (1996), and Mei et al. (2001), in order to obtain reliable SBF measurements in the IR, the $S/N \equiv (P_0 - P_r)/P_1 = P_f/P_1$ must be $\gtrsim 5$. The conclusions of these authors agree with Blakeslee et al. (1999) who, from an observational point of view, provided the equation to predict SBF S/N ratio, suggesting to keep this value above 5-10. As shown in Table 2, the I-band S/N measured from our data is $\gtrsim 20$, while for B-band images it can be as low as ~ 2.6 , and it is ~ 5.7 in the best case. In this section we present various consistency tests useful to verify the reliability of our SBF measurements procedure in such low S/N regimes.

As a first check, we developed a procedure capable of simulating realistic CCD images of galaxies with known input SBF magnitudes derived using SSP models, then we measured the SBF of the simulated image to verify the matching with the input SBF value. In order to properly simulate the properties of our real images, the simulations also included external sources, and the instrumental noise of the camera. A detailed description of the simulations is reported in Appendix A.

To check the consistency of the measured SBF signal with the input one as a function of the S/N ratio of the image, we have performed two different tests adopting two distance moduli for the galaxy ($\mu_0=32, 33$), changing the exposure time in a wide range for each distance modulus. To properly take into account the role of the P_r correction, we have assumed the luminosity functions of globular clusters and background galaxies according to the average properties of our ACS images. The results of this study are reported in Figure 3. In the figure we show the input SBF magnitudes (shaded areas; models are from the Teramo SPoT group²), the SBF measured in the simulated frame before adding external sources (empty stars), and the SBF magnitudes measured after including also external sources (filled circles). From these panels can be recognized that the measured SBF agree with the input signal within uncertainty, but the uncertainty strongly increases at low exposure times, i.e. low S/N, since the residual sources P_r and the white noise P_1 components dominate the total fluctuation amplitude. The properties of the observational data used for this work are

²The Teramo “Stellar POpulations Tools” (SPoT) models, from Raimondo et al. (2005), are available at the URL: www.oa-teramo.inaf.it/SPoT

also shown in the Figure 3 with boxes located in the regions corresponding to the proper exposure times (only objects at the correct distance have been considered for each panel). In conclusion, these simulations show that our SBF measurements procedure works well on CCD images having *average* properties similar to our sample of ACS images. However, it must be pointed out that each single galaxy of the present sample has different characteristics (amount of external sources, effective area for the SBF analysis, etc.), which can affect the SBF estimation in each specific case.

As a further check of the measurements quality, we have obtained SBF measurements versus the exposure time for real data, by degrading the original high S/N images to simulate shorter exposure time and smaller SBF S/N ratio. For this test we have used NGC 5557 data, splitting the images of both bands available in three different exposure times: total exposure time ($S/N \lesssim 6$), $2/3$ ($S/N \lesssim 4$), and $1/2$ ($S/N \lesssim 3$) of the total exposure time. As a result we find that the I-band SBF measurements are left practically unchanged, as there is less than 0.1 mag difference between the two extreme exposure times. On the contrary, the B-band image with the lowest exposure time ($S/N < 3$) has too bright SBF, as $\bar{m}_B \sim 34.6 \pm 0.3$ compared to the original $\bar{m}_B \sim 35.2 \pm 0.3$. Both B- and I-band SBF amplitudes measured from the $2/3$ exposure time frames agree within uncertainty with the original measurement.

In conclusion, we adopt the value $S/N \sim 3$ as limit of separation between unreliable and reliable SBF measurements for F435W ACS images. With this choice, we are lead to consider as reliable (within the quoted uncertainties) the B-band SBF data for NGC 4696, NGC 5322 and NGC 5557, while NGC 3258 and NGC 3268 both lie on the limit of reliability and NGC 1407 is below. In the next sections, the B-band SBF measurement for the last three galaxies will be quoted but not considered in the analysis and in the discussion.

4. Discussion

The common use of SBF magnitudes as a distance indicator relies on the tight dependence of fluctuations amplitudes on the properties of stellar populations in galaxies. However, SBF brightness dependence on stellar population depends on the wavelength interval considered. Theoretical studies have shown that SBF measured in filters like B are not good distance indicators because one parameter (i.e. integrated color) is not sufficient to describe the stellar population of galaxies, but they are appropriate for stellar populations analysis. As discussed by several authors (e.g., Worthey 1993a; Sodemann & Thomsen 1996; Cantiello et al. 2003; Raimondo et al. 2005), B-band SBF magnitudes can be strongly affected by the light coming from hot luminous stars (extreme HB, Post-AGB, young MS stars, etc.).

The limited number of observational data in the B-band up to now hampered the ability to check the validity of model SBF predictions. Furthermore, the available data mainly refer to galaxies at distances lower than 5 Mpc: M32 (Sodemann & Thomsen 1996), and NGC 5128 (Shopbell et al. 1993). These two galaxies will be added to our sample of objects in the following section. The \bar{m}_I value for NGC 5128 comes from the Tonry et al. (2001) database. All the data adopted for M32, and NGC 5128 are reported in Table 3. The $(B - I)_0$ color for these galaxies is obtained using the C05 color transformations, upgraded with the new Raimondo et al. (2005, R05) models.

The measurements presented in this paper increase the sample of B-band SBF data, and they are the first for a sample of distant giant elliptical galaxies. Within the limits of the low S/N of the B-band SBF data, in the following sections we compare B- and I-band SBF magnitudes and colors with models predictions, in order to point out the capabilities of blue band SBF as an inquiry tool for stellar populations, especially in view of applications (\bar{B} radial gradients, \bar{B} -near-IR color data, etc.) based on future high-S/N imaging data.

4.1. Observational properties and comparison with standard SSP models

In this section we discuss some characteristics of the SBF data for our sample of objects in the light of most recent and detailed SBF model predictions. It is important to emphasize that the forthcoming comparison is only a “first approximation” approach to the general problem of inferring the physical properties of the stellar populations generating the SBF signal.

As a first step, we will make use of upgraded and reliable R05 models which – within the same consistent theoretical framework – have been proved to reproduce in detail the color-magnitude diagrams, the integrated magnitudes and colors and SBF of well studied systems (e.g. galactic globulars and MC star clusters) and elliptical galaxies. Even so, one should keep in mind that SBF predictions include the uncertainties and assumption (IMF, color transformation, evolutionary tracks, etc.) that typically affect the theoretical stellar population synthesis models. Thus, taking into account the observational uncertainties and the small number of galaxies observed, the present discussion should be considered as an exploration of the capabilities of SBF method in the B-band more than a detailed comparison of models with data.

In Figure 4 we compare SBF and color data with the recent R05 SSP models. The upper two panels in Figure 4 show the \bar{M}_I and \bar{M}_B versus the galaxy integrated color. Absolute SBF magnitudes are derived using the distance moduli reported in Table 3. SBF color data

and models are shown in the lower panel. In this Figure we plot with different symbols the reliable data (full circles), and the B-band unreliable data (empty circles). Also the data of M32 and NGC5128 are reported (filled triangles). For completeness and, additionally, to emphasize possible inhomogeneities emerging between the different bands, in the following paragraphs we will analyze the galaxy properties emerging from each one of the panels in Figure 4.

- \bar{M}_I versus $(B - I)_0$ – I-band comparison of the models to the data shows excellent agreement of R05 SBF models with SBF measurements. This result substantially support the finding presented in C05, even though here we are discussing one single averaged SBF measurement, instead of SBF gradients. Specifically, an old $t \gtrsim 10$ Gyr, metal rich $Z \gtrsim 0.02$ stellar population dominates the light emitted by these galaxies.

For the case of M32, SBF data are well reproduced by R05 SSP models with an age ~ 5 Gyr and $Z \lesssim 0.02$. This result is very similar to what found by Cantiello et al. (2003), and by other authors (e.g., Trager et al. 2000) from line strength analysis.

NGC5128 (Centaurus A) data are consistent with SSP models having $t \gtrsim 3$ Gyr, and $Z \lesssim 0.02$. The average metallicity inferred from resolved halo stars is $Z \gtrsim 0.005$, with a large spread; two age peaks are recognized, one at 2 Gyr and one at older ages (Marleau et al. 2000). Moreover, the complexity of the NGC5128 stellar system increases as one approaches the regions of the dark absorption lanes in the galaxy (Rejkuba et al. 2001). Note that the resolved stars data refer to regions not overlapping with the SBF data measured closer to the center of the galaxy. Broad band colors in regions overlapping ours have been derived by several authors (van den Bergh 1976; Dufour et al. 1979). These authors settled the twofold character of the NGC5128 stellar populations, with a main body component which is old but bluer than usual in elliptical galaxies, consistent with a 7-9 Gyr, $Z \sim 0.01$ stellar system, and a disk of young, metal rich stars. In conclusion, taking into account the complexity of the stellar system of NGC5128, and the integrated nature of the SBF signal data, we consider as satisfactory the agreement between the properties of stellar systems inferred from SBF versus color data/models comparisons and properties taken from literature.

- \bar{M}_B versus $(B - I)_0$ – Inspecting the middle panel of Figure 4 we find that the B-band SBF magnitudes are brighter than the model predictions, in contrast to the good agreement obtained with the I-band. The only exception being NGC5128 (and NGC3268 which, however, we consider at the limit of reliability) due to the big error bars. All the galaxies at $(B - I)_0 \gtrsim 2.1$ mag appear to have substantially brighter SBF magnitudes respect to models predictions.

Also in the case of M 32 the age and chemical composition derived from this panel do not agree with properties inferred from I-band SBF or literature data. Again, the SBF measured is brighter respect to models expectations for a $t \sim 5$ Gyr $Z \sim 0.02$ stellar system.

- $(\bar{B} - \bar{I})$ versus $(B - I)_0$ – The additional distance modulus uncertainty present in the top two panels of Figure 4, is removed in the bottom SBF-color versus color panel. However, as shown in this panel, no substantial improvement occurs by using the distance-free SBF-color versus integrated color with respect to the disagreement presented before.

To analyze the possible origin of the mismatch when the B-band data are considered, we have compared our SBF and color data with other sets of stellar population models (Worthey 1994; Blakeslee et al. 2001; Marín-Franch & Aparicio 2006, Figure 5 shows the latter two set of models). However, adopting different SBF models does not solve the mismatch in the B-band. This is quite interesting because it can be interpreted (within the quoted small statistics and wide observational error bars) as an indication of a missing contributor to the SBF signal in the canonical B-band SSP models. A further possibility is the eventuality of a systematic bias of the B-band measurements which may explain the disagreement without requiring implication of the SSP models. On the basis of extended experiments with simulations we are leaded to discard the presence of systematic offsets in the B-band data. However, this hypothesis could not be ruled out due to the small statistics of our sample.

4.2. Comparison with non-standard SSP models

A possible alternative to understand such B-band data/models disagreement is to consider non standard stellar population models. As examples of non standard models, we take into account two different cases: (i) SSP models with a non standard ratio of Post-AGB to HB number of stars; (ii) SBF models of Composite Stellar Populations (CSP).

(i) Following the discussion concerning the contribution to SSP of hot stars experiencing bright and fast evolutionary phases presented by Brocato et al. (1990, 2000), and taking into account the Worthey (1993a) comments on the effects of these stars on SBF magnitudes, in Cantiello et al. (2003) we presented a detailed analysis of the SBF magnitudes against the number of hot stars in the late evolutionary phases (Post-AGB). In that work it is shown that SSP models with an increased ratio of the number of Post-AGB stars with respect to the number of HB stars ($N_{Post-AGB}/N_{HB}$), have brighter \bar{M}_B amplitudes, while the \bar{M}_I and colors are left practically unchanged.

In Figure 6 we show the comparison of the models to the data adopting SSP models with a $N_{Post-AGB}/N_{HB}$ ratio doubled with respect to standard models. As can be recognized from the Figure, all the stellar populations properties inferred from the B-band models agree, within the observational error bars, with the same I-band models described above, except for the NGC 5557 data. This means that SSP models which include a component of hot, bright stars undetectable in the SBF I-band models, but with a non negligible effect on B-band SBF measurements, is able to reconcile the mismatch we find between standard SSP models and B-band measurements.

(ii) B-band SBF amplitudes may reveal the presence of populations of hot stars (extreme HB stars, post-AGB stars, young populations, metal-poor stars, etc.), even when they only represent a small fraction of the overall stellar population. B-band SBFs are therefore a valuable tool to investigate Composite Stellar Population. As shown by C05, in some cases the combination of a dominant stellar population with secondary hot components of different chemical compositions and/or ages, eventually allows to better explain some observational properties of the galaxy. For this comparison we adopt the Blakeslee et al. (2001, BVA01 hereafter) CSP models, thus our conclusions must be considered as valid only within the limits of such CSP scenario. The BVA01 CSP models are obtained combining homogeneous SSP models in such a way as to mimic, at least approximately, the evolution of an elliptical galaxy. We refer the reader to the BVA01 paper for a detailed description of their composite models. Briefly: SSP models are grouped into three bins according to metallicity: metal-poor ($0.0004 \leq Z \leq 0.001$, m.p. hereafter), intermediate ($0.004 \leq Z \leq 0.008$, int.), and metal-rich ($0.02 \leq Z \leq 0.03$, m.r.). Then one SSP model is randomly chosen from each metallicity bin, with some age restrictions depending on the bin. The three components are then combined according to random weighting factors $[f_{m.p.}, f_{int.}, f_{m.r.}]$, and fluctuation amplitudes calculated using a generalization of the Tonry & Schneider formula.

In Figure 7 the comparison of these models with observational data is presented. In the Figure we mark the edges of the area covered by models. As shown in the panels of the Figure, the presence of CSP eliminates the problems existing with previous standard SSP models, as all data lie within the area of the models. By inspecting the average properties of CSP models overlapping with observational data, one concludes that:

- the galaxies at $(\bar{B} - \bar{I})_0 \sim 3.4$ mag and $(B - I)_0 \sim 2.2$ mag are strongly dominated by an old ($t \gtrsim 14$ Gyr) metal rich stellar system, with a possible minor contribution due to an intermediate metallicity stellar component ($f_{int.} \lesssim 20\%$), and a negligible amount of a metal-poor component ($f_{m.p.} \lesssim 5\%$)
- M 32 data agree with CSP models composed by a comparable fraction of a metal-rich stellar system of 5-7 Gyr, and an intermediate metallicity population with $t \sim 11$ Gyr.

- NGC 5128 is the only case where the dominant component is not the metal-rich one. In this case a $t \sim 9$ Gyr, intermediate metallicity stellar system appears to be the dominant stellar component ($f_{int.} \sim 60\%$), with a secondary $t \sim 7$ Gyr metal-rich one.
- for NGC 5322 observational data overlap with models having $\sim 70\%$ of light coming from a metal-rich $t \sim 13$ Gyr component, and a substantial fraction of light coming from an intermediate metallicity ($f_{int.} \sim 20\%$), and a metal-poor ($f_{m.p.} \sim 10\%$) component. A similar result is found for NGC 5557, with the difference that the metallicity of the most metal poor component in this case is $Z \sim 0.0004$.

In addition to the two previous non-standard SSP models, we have also considered the case SSP obtained using α -enhanced stellar tracks, based on the recent models by Lee et al. (2006). The use of α -enhanced SBF/color models lead to estimate chemical compositions which are on average a factor 0.3 dex higher respect to our previous conclusions, with substantially unchanged ages, but the mismatch aforementioned is not reconciled. Thus we can exclude the α -enhancement as the driving source of the B-band mismatch, at least within the limit of the scenario presented by Lee et al. (2006).

Although the above conclusions must not be over interpreted and considered as valid only within the limits of the specific non-standard models taken into account and the low S/N of the B-band SBF data, these results possibly point out that (i) I-band SBF magnitudes are confirmed as a powerful distance indicator, as they exhibit a small dependence on the detailed properties of the stellar population in the galaxy; (ii) B-band SBF amplitudes are sensibly affected by also a small component of a hot stellar system (extreme HB stars, Post-AGB stars, young populations, metal-poor components, etc.) and represent a valuable tool to study the presence of these stars and/or stellar populations in unresolved stellar systems.

5. Conclusions

In this paper we have carried out the first extensive study on B-band SBF measurements for distant galaxies, based on measurements obtained from ACS imaging data for a sample of six elliptical galaxies. In a previous paper (C05) we succeeded in detecting I-band SBF radial gradients for the same sample of objects. The quality of B-band images did not allow us to obtain SBF measurements in different galaxy regions. Moreover, after a few image tests, we have decided that only three of these B-band SBF measurements could be considered as reliable.

We have added to our sample the only two other galaxies with I- and B-band SBF measurements available from literature: M 32 and NGC 5128. The analysis of the observational

properties of this sample of galaxies shows that using the standard SSP models from the SPoT group, and various models from other authors, the stellar population properties derived from I-band SBF versus $(B - I)_0$ color data/models comparison agree with the stellar population properties known in literature derived from other indicators. Briefly: the most massive objects appear to be dominated by an old ($t \gtrsim 10$ Gyr) metal-rich $Z \gtrsim 0.02$ stellar component; M32 light is dominated by a $t \sim 5$ Gyr $Z \sim 0.02$ stellar system, while NGC5128 light seems to be dominated by a $t \sim 3$ Gyr, $Z \gtrsim 0.01$ population.

In spite of this, we find that the B-band comparison of the models to the data is not satisfactory, especially for the red [$(B - I)_0 \gtrsim 2.1$] galaxies in our sample. In order to try to solve such disagreement we have presented a comparison of data with non standard stellar population models. In particular we have used prescriptions based on two different approaches. (i) Models with an enhanced number of hot (Post-AGB) stars: these models appear to resolve almost completely the disagreement present with the standard SSP models, within the limit of the observational uncertainty. The only galaxy whose properties do not seem to be well interpreted in this scenario is NGC5557. (ii) Composite Stellar Population models: within this scenario the SBF measurements are all included in the region of the SBF-color diagrams covered by the CSP models. In particular, these models show that the light of the galaxies in our sample at $(B - I)_0 \gtrsim 2.1$ mag can be interpreted as dominated by an old, $t \gtrsim 10$ Gyr, $Z \gtrsim 0.02$ stellar component, in some cases accompanied by a non negligible amount of lower metallicity stellar components. As an example, NGC5557 data are nicely reproduced by models including a small fraction ($\sim 10\%$ of the total light) of old $Z \sim 0.0004$ stars.

In conclusion, our results confirm the theoretical expectations that \bar{B} data are not well suited for distance study and, together with SBF colors like the $\bar{B} - \bar{I}$, they represent a valuable tool to investigate the properties of unresolved stellar systems, with particular regard to the hot stellar component. As a concluding remark, we emphasize that the use of B-band SBF, SBF-color, and SBF radial gradients data to study the properties of the stellar systems of external galaxies, rely on the availability of high quality observational data. The data used for this work are generally characterized by low S/N ratios, based on the simulations and results presented in this paper for B-band SBF, we suggest that higher S/N data ($S/N \gtrsim 10$) is required to carry out a detailed study of stellar population properties based on this technique.

Financial support for this work was provided by COFIN 2004, under the scientific project “Stellar Evolution” (P.I.: Massimo Capaccioli).

A. Simulating “realistic” CCD images of elliptical galaxies

In this appendix we outline the major steps of the procedure to simulate CCD images of elliptical galaxies adopted in section 3. The procedure has been properly developed to include the SBF signal in the galaxy model.

One of the basic inputs of these simulations is the R05 SSP models, which fix the chemical content and the age of the SSP for each simulation. One of the capabilities of the SPoT stellar synthesis code is to generate N_{sim} independent simulations of SSP with fixed age and metallicity. Once the SSP total mass is fixed, the SPoT code is able to randomly populate the IMF of the stellar system. The code is implemented to reliably simulate stars on all post-MS phases: RGB, HB, AGB, etc.; see Brocato et al. (1999, 2000) and Raimondo et al. (2005) for the details. At fixed age, metallicity, and IMF shape, the simulations obtained have, on average, similar properties (according to the average mass of the population), but each single simulation differs from the others for statistical reasons.

We use such capability (1) to simulate a “realistic” galaxy, which also includes the SBF signal, whose amplitude is fixed by the input properties of the SSP. Then, (2) we measure fluctuations amplitudes of the simulated galaxy applying the procedure described in section 2.2.3. Finally, (3) the SBF measured is compared with the input one to verify if and how, in the case of low S/N images, the measurements are affected.

First of all, we simulate a galaxy with a de Vaucouleurs (1948) $r^{1/4}$ luminosity profile, although the procedure accepts also a generic Sersic (1968) $r^{1/n}$ profile. Starting from the smooth *analytic profile* whose SBF is zero, we built a *realistic profile* to simulate the poissonian fluctuation due the star counts which, as mentioned before, constitutes the physical basis of the SBF signal. To simulate the fluctuations, at each fixed radius r_* , we substitute the well defined analytic surface brightness $\mu(r_*)_{an}$ in all N_{pix} pixels corresponding to this radius, with the surface brightness of a simulated SSP belonging to a sample of N_{pix} SSP simulations having $\langle \mu(r_*)_{SSP} \rangle = \mu(r_*)_{an}$, in this way the brightness profile of the galaxy is preserved and the poissonian fluctuation due to star count fluctuation is included.

This procedure (which is repeated at all radii) requires a large number of SSP models, according to the number or radii one wants to simulate. We note once more that, since the SSP is chosen by the user, the galaxy SBF amplitude is an input parameter; for example by using the R05 models for an SSP having $Z=0.02$ and $t = 14$ *Gyr*, the input SBF is $\bar{M}_B \sim 2.9$ in B-band, or $\bar{M}_I \sim -1.2$ in case of I-band simulations.

At this point, to simulate fully realistic CCD image, we included the effect of the PSF, external sources (globular clusters and galaxies), and instrumental noise. To simulate the effect of the PSF on the data, the galaxy image is convolved with the point spread function

profile before adding the external sources (which are already convolved with the instrumental PSF). The external sources were added according to a fixed total luminosity function of globular clusters and galaxies. This luminosity function, similar to those shown in Figure 2, is of the sum of a power law for galaxies, and a GCLF. Galaxies are randomly distributed on the galaxy image, Globular Clusters were distributed using an inverse power law centered on the galaxy. A constant sky value is also added to the image. Finally the photon and detector noises are added by using the IRAF task *mknoise*, according to the readout-noise and gain properties of ACS.

It must be emphasized that, in addition to the input parameters already introduced (galaxy profile index, density and spatial distribution of GCs, density of background galaxies, PSF shape, age and metallicity of the SSP), there are also some other user-defined parameters in the galaxy simulation which are not discussed here (distance, effective magnitude and effective radius, exposure time, field of view, zero point magnitude, sky brightness, etc.).

Once the simulation has been completed, the whole procedure described in section 2.2.3 (sky evaluation, galaxy modeling, sources detection and masking, LF fitting, SBF measurement) is run on the simulated CCD images.

In order to show the effect of introducing the Poissonian variation between adjacent pixels, in Figure 8 we show the power spectrum of the residual frames for an image simulated with (right panel), and without (left panel) the SBF signal. The difference clearly emerges: the spectrum of the image without SBF is flat (i.e., no SBF signal is revealed), while the power spectrum of the image with SBF has the characteristic PSF shape.

We thank the anonymous referee for helping us to improve this paper with constructive criticisms and useful suggestions.

REFERENCES

Ajhar, E. A., & Tonry, J. L. 1994, ApJ, 429, 557

Benítez, N. et al. 2004, ApJS, 150, 1

Bertelli, G., Bressan, A., Chiosi, C., Fagotto, F., & Nasi, E. 1994, A&AS, 106, 275

Bertin, E., & Arnouts, S. 1996, A&AS, 117, 393

Blakeslee, J. P., Ajhar, E. A., & Tonry, J. L. 1999, in ASSL Vol. 237: Post-Hipparcos cosmic candles, 181

Blakeslee, J. P., Anderson, K. R., Meurer, G. R., Benítez, N., & Magee, D. 2003, in ASP Conf. Ser. 295: Astronomical Data Analysis Software and Systems XII

Blakeslee, J. P., & Tonry, J. L. 1995, *ApJ*, 442, 579

Blakeslee, J. P., Vazdekis, A., & Ajhar, E. A. 2001, *MNRAS*, 320, 193 (BVA01)

Brocato, E., Castellani, V., Poli, F. M., & Raimondo, G. 2000, *A&AS*, 146, 91

Brocato, E., Castellani, V., Raimondo, G., & Romaniello, M. 1999, *A&AS*, 136, 65

Brocato, E., Matteucci, F., Mazzitelli, I., & Tornambe, A. 1990, *ApJ*, 349, 458

Buzzoni, A. 1993, *A&A*, 275, 433

Cantiello, M., Blakeslee, J. P., Raimondo, G., Mei, S., Brocato, E., & Capaccioli, M. 2005, *ApJ*, 634, 239 (C05)

Cantiello, M., Raimondo, G., Brocato, E., & Capaccioli, M. 2003, *AJ*, 125, 2783

de Vaucouleurs, G. 1948, *Annales d'Astrophysique*, 11, 247

Dufour, R. J., Harvel, C. A., Martins, D. M., Schiffer, III, F. H., Talent, D. L., Wells, D. C., van den Bergh, S., & Talbot, Jr., R. J. 1979, *AJ*, 84, 284

Ferrarese, L. et al. 2000, *ApJ*, 529, 745

Ferrarese, L., Mould, J. R., Stetson, P. B., Tonry, J. L., Blakeslee, J. P., & Ajhar, E. A. 2007, *ApJ*, 654, 186

González, R. A., Liu, M. C., & Bruzual A., G. 2004, *ApJ*, 611, 270

Harris, W. E. 1991, *ARA&A*, 29, 543

Harris, W. E. 2001, in Saas-Fee Advanced Course 28: Star Clusters

Jacoby, G. H. et al. 1992, *PASP*, 104, 599

Jensen, J. B., Luppino, G. A., & Tonry, J. L. 1996, *ApJ*, 468, 519

Jensen, J. B., Tonry, J. L., Barris, B. J., Thompson, R. I., Liu, M. C., Rieke, M. J., Ajhar, E. A., & Blakeslee, J. P. 2003, *ApJ*, 583, 712

Jensen, J. B., Tonry, J. L., Thompson, R. I., Ajhar, E. A., Lauer, T. R., Rieke, M. J., Postman, M., & Liu, M. C. 2001, *ApJ*, 550, 503

Jerjen, H., Freeman, K. C., & Binggeli, B. 1998, AJ, 116, 2873

—. 2000, AJ, 119, 166

Lee, H.-c., Worthey, G., & Blakeslee, J. P. 2006, American Astronomical Society Meeting Abstracts, 208, 10.07

Liu, M. C., Charlot, S., & Graham, J. R. 2000, ApJ, 543, 644

Marín-Franch, A., & Aparicio, A. 2006, A&A, 450, 979

Marleau, F. R., Graham, J. R., Liu, M. C., & Charlot, S. 2000, AJ, 120, 1779

Mei, S., Silva, D. R., & Quinn, P. J. 2001, A&A, 366, 54

Mieske, S., & Hilker, M. 2003, A&A, 410, 445

Mouhcine, M., González, R. A., & Liu, M. C. 2005, MNRAS, 362, 1208

Press, W. H., Teukolsky, S. A., Vetterling, W. T., & Flannery, B. P. 1992, Numerical recipes in FORTRAN. The art of scientific computing (Cambridge: University Press, —c1992, 2nd ed.)

Raimondo, G., Brocato, E., Cantiello, M., & Capaccioli, M. 2005, AJ, 130, 2625 (R05)

Rejkuba, M., Minniti, D., Silva, D. R., & Bedding, T. R. 2001, A&A, 379, 781

Schlegel, D. J., Finkbeiner, D. P., & Davis, M. 1998, ApJ, 500, 525

Sersic, J. L. 1968, Atlas de galaxias australes (Cordoba, Argentina: Observatorio Astronomico, 1968)

Shopbell, P. L., Bland-Hawthorn, J., & Malin, D. F. 1993, AJ, 106, 1344

Sirianni, M. et al. 2005, PASP, 117, 1049

Sodemann, M., & Thomsen, B. 1995, AJ, 110, 179

—. 1996, AJ, 111, 208

Stetson, P. B. 1990, PASP, 102, 932

Tonry, J., & Schneider, D. P. 1988, AJ, 96, 807

Tonry, J. L. 1991, ApJ, 373, L1

Tonry, J. L., Ajhar, E. A., & Luppino, G. A. 1989, *ApJ*, 346, L57

—. 1990, *AJ*, 100, 1416

Tonry, J. L., Dressler, A., Blakeslee, J. P., Ajhar, E. A., Fletcher, A. B., Luppino, G. A., Metzger, M. R., & Moore, C. B. 2001, *ApJ*, 546, 681

Trager, S. C., Faber, S. M., Worthey, G., & González, J. J. 2000, *AJ*, 120, 165

Tyson, J. A. 1988, *AJ*, 96, 1

van den Bergh, S. 1976, *ApJ*, 208, 673

Worthey, G. 1993a, *ApJ*, 415, L91

—. 1993b, *ApJ*, 409, 530

—. 1994, *ApJS*, 95, 107

Table 1. Observational Data

Galaxy	R.A.	Decl.	v_{cmb} (km/s)	T	A_B	F814W exp. time(s)	F435W exp. time (s)
(1)	(2)	(3)	(4)	(5)	(6)	(7)	(8)
NGC 1407	55.052	-18.581	1627	-5	0.297	680	1500
NGC 3258	157.226	-35.606	3129	-5	0.363	2280	5360
NGC 3268	157.503	-35.325	3084	-5	0.444	2280	5360
NGC 4696	192.208	-41.311	3248	-4	0.489	2320	5440
NGC 5322	207.315	60.191	1916	-5	0.061	820	3390
NGC 5557	214.605	36.494	3433	-5	0.025	2400	5260

Notes Col. (1): Galaxy name; Cols. (2) and (3): Right ascension and declination from RC3; Col. (4): Recession velocity in the CMB reference frame from Tonry et al. (2001); Col. (5): Morphological T-type from RC3; Col. (6): B-band extinction from Schlegel et al. (1998); Col. (7) and (8): total exposure time for F814W and F435 images, respectively.

Table 2. Fitting Parameters

Galaxy (1)	r(arcsec) (2)	B-band fitting parameters (ADU/exposure)					I-band fitting parameters (ADU/exposure)				
		P_0 (3)	P_1 (4)	P_r (5)	P_f (6)	S/N (7)	P_0 (8)	P_1 (9)	P_r (10)	P_f (11)	S/N (12)
NGC 1407	13 3 26	0.67 ± 0.02	0.17	0.22	0.45	2.6	3.93 ± 0.07	0.14	0.29	3.64	25
NGC 3258	13 6 20	0.99 ± 0.10	0.19	0.39	0.59	3.2	5.61 ± 0.20	0.12	0.27	5.34	43
NGC 3268	12 6 20	0.85 ± 0.11	0.16	0.40	0.46	2.9	5.72 ± 0.08	0.11	0.25	5.46	49
NGC 4696	14 6 20	0.84 ± 0.13	0.11	0.42	0.43	4.0	5.30 ± 0.19	0.07	0.26	5.04	73
NGC 5322	15 6 26	0.94 ± 0.05	0.21	0.10	0.84	4.0	4.43 ± 0.06	0.18	0.18	4.26	23
NGC 5557	12 3 20	0.93 ± 0.04	0.14	0.12	0.81	5.7	5.37 ± 0.20	0.13	0.18	5.19	40

Notes Col. (1): Galaxy; Col. (2) average annular radius, innermost mask radius, outermost mask radius; Col. (3-6) P_0 , P_1 , P_r and P_f estimated for B-band images; Col. (7) S/N evaluated as $(P_0 - P_r)/P_1$ for B-band frames; Col. (8-11) P_0 , P_1 , P_r and P_f estimated for I-band images; Col. (12) S/N for I-band frames.

Table 3. Observational data

Galaxy (1)	$\mu_{0,Group}$ (2)	B_t (3)	$(B-I)_0$ (4)	$\bar{m}_{B,0}$ (5)	$\bar{m}_{I,0}$ (6)
NGC 1407	32.01 ± 0.06	10.71 ± 0.18	2.237 ± 0.033	34.3 ± 0.2	31.08 ± 0.07
NGC 3258	32.85 ± 0.11	12.52 ± 0.13	2.189 ± 0.032	35.3 ± 0.3	31.95 ± 0.06
NGC 3268	32.85 ± 0.11	12.30 ± 0.44	2.189 ± 0.032	35.5 ± 0.3	31.90 ± 0.06
NGC 4696	32.95 ± 0.05	11.62 ± 0.30	2.239 ± 0.033	35.5 ± 0.4	31.99 ± 0.07
NGC 5322	32.48 ± 0.11	11.04 ± 0.22	2.105 ± 0.031	34.7 ± 0.1	31.22 ± 0.07
NGC 5557	33.45 ± 0.11	11.92 ± 0.10	2.145 ± 0.032	35.2 ± 0.1	32.17 ± 0.08
Data taken from literature					
Galaxy	$\mu_{0,Group}$	B_t	$(V-I)_0$	$\bar{m}_{B,0}$	$\bar{m}_{I,0}$
M 32	24.45 ± 0.04	8.87 ± 0.35	1.133 ± 0.007	26.78 ± 0.03	22.78 ± 0.04
NGC 5128	27.67 ± 0.12	7.96 ± 0.26	1.078 ± 0.016	30.1 ± 0.5	26.05 ± 0.11

Notes Col. (1): Galaxy name; Col. (2) Distance modulus derived averaging the group μ_0 estimations of FP and IRAS velocity maps distribution (Table 6 data in C05). For NGC 5557 no group distance is known, we adopt the weighted average distance of various μ_0 estimated for the galaxy itself. M 32 distance is derived as weighted averages of group distances from the Ferrarese et al. (2000) database, excluding SBF based distances. NGC 5128 distance comes from Ferrarese et al. (2007), based on Cepheids variables. Col. (3) : apparent total B magnitude and uncertainty from Hyperleda Catalogue (URL: <http://leda.univ-lyon1.fr>); Col. (4): $(B - I)_0$ integrated color; Col. (5)-(6): B- and I-band SBF apparent magnitudes.

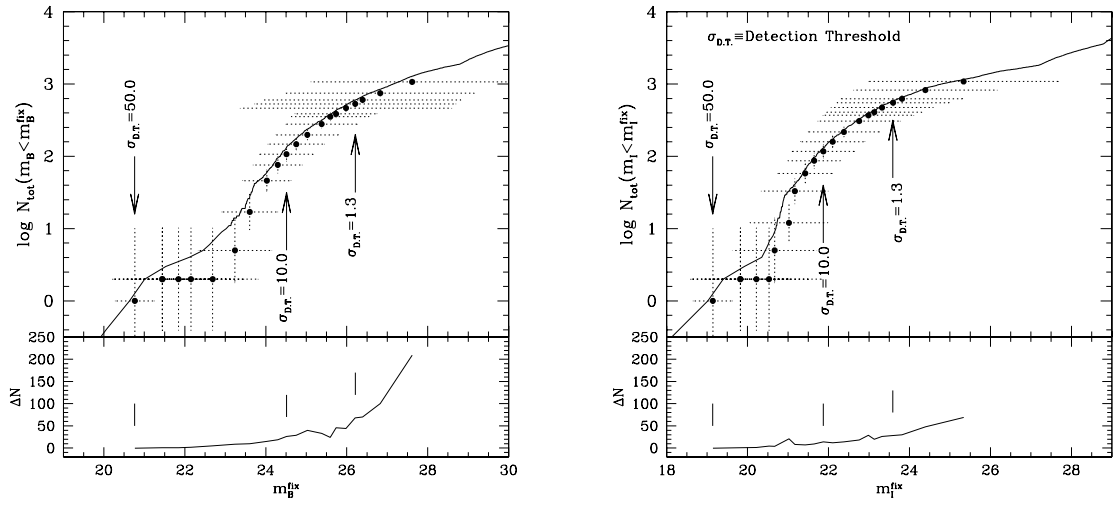


Fig. 1.— *Upper panels* - The number of sources detected (globular clusters+galaxies) brighter of the magnitude m^{fix} , versus the magnitude m^{fix} itself. We defined the latter quantity as the average magnitude of the sources detected for the specific $\sigma_{D.T.}$ adopted. Left (right) panels exhibits the results of this test for B-band (I-band) simulations. Full dots refer to the total number of objects detected on the frame simulated, the solid line shows the input total integrated luminosity function adopted for the simulations. *Lower panels* - The differences between the number of detected objects brighter than m^{fix} , and the real number of objects adopted for the simulation: $\Delta N = |N_{detected} - N_{input}|$.

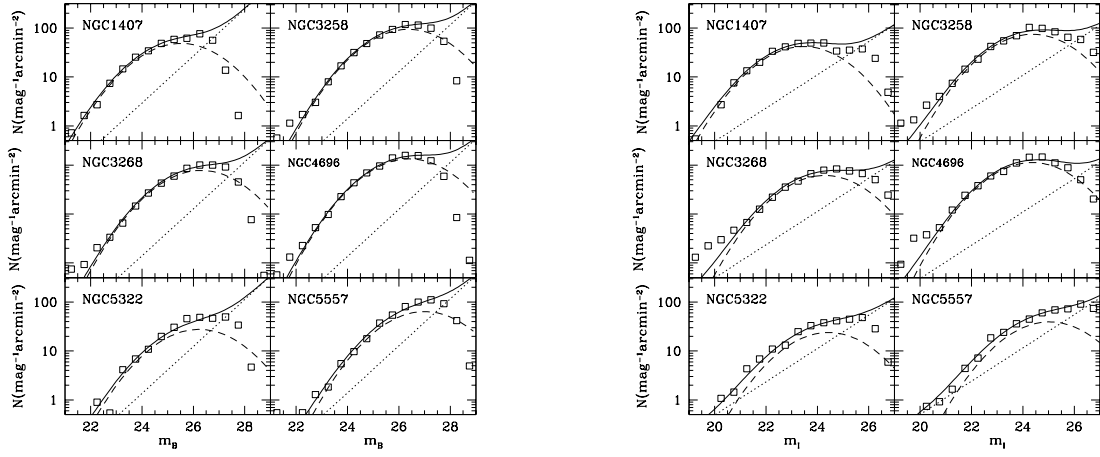


Fig. 2.— The B-band (left panels) and I-band (right panels) total luminosity function of external sources. The panels show the observed total number density as a function of the magnitude (open squares), and the model luminosity function used to estimate the residual contribution to fluctuations arising from undetected sources (solid line). The two components of the model number density, globular clusters and background galaxies, are also shown with dashed and dotted lines, respectively.

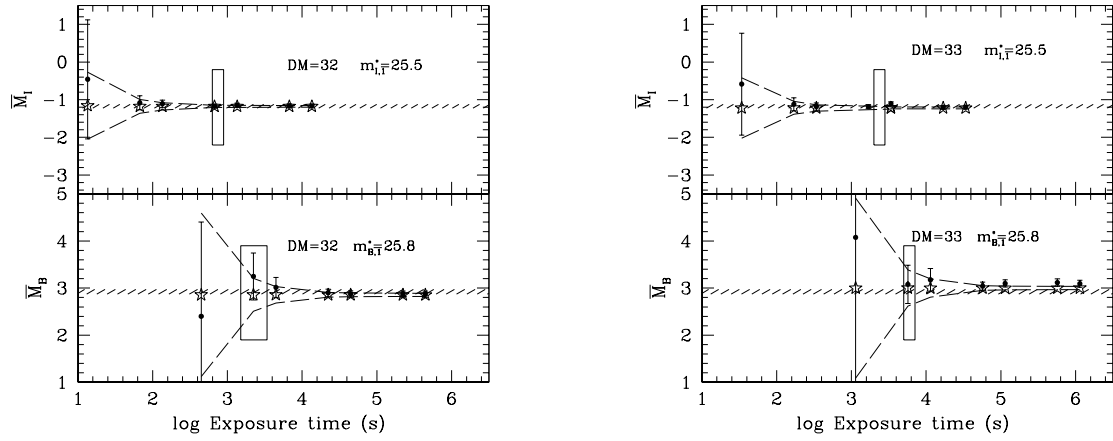


Fig. 3.— *Left panel* - Absolute SBF magnitudes measured for the galaxy simulated at distance modulus $\mu_0=32$ against the exposure time adopted for the simulation. Open stars mark the SBF measured from the frame without external sources, i.e. the P_r term is zero ($1-\sigma$ area is also shown with long-dashed lines). Full dots mark the SBF measured from the final image: it can be recognized that adding external sources causes a higher dispersion of data and higher uncertainties at lower exposure times. The shaded horizontal area refers the input SBF signal. Finally, the boxes locate the positions of our observational data, for those galaxies at $\mu_0 \sim 32$. *Right panel* - As left panel but for $\mu_0=33$.

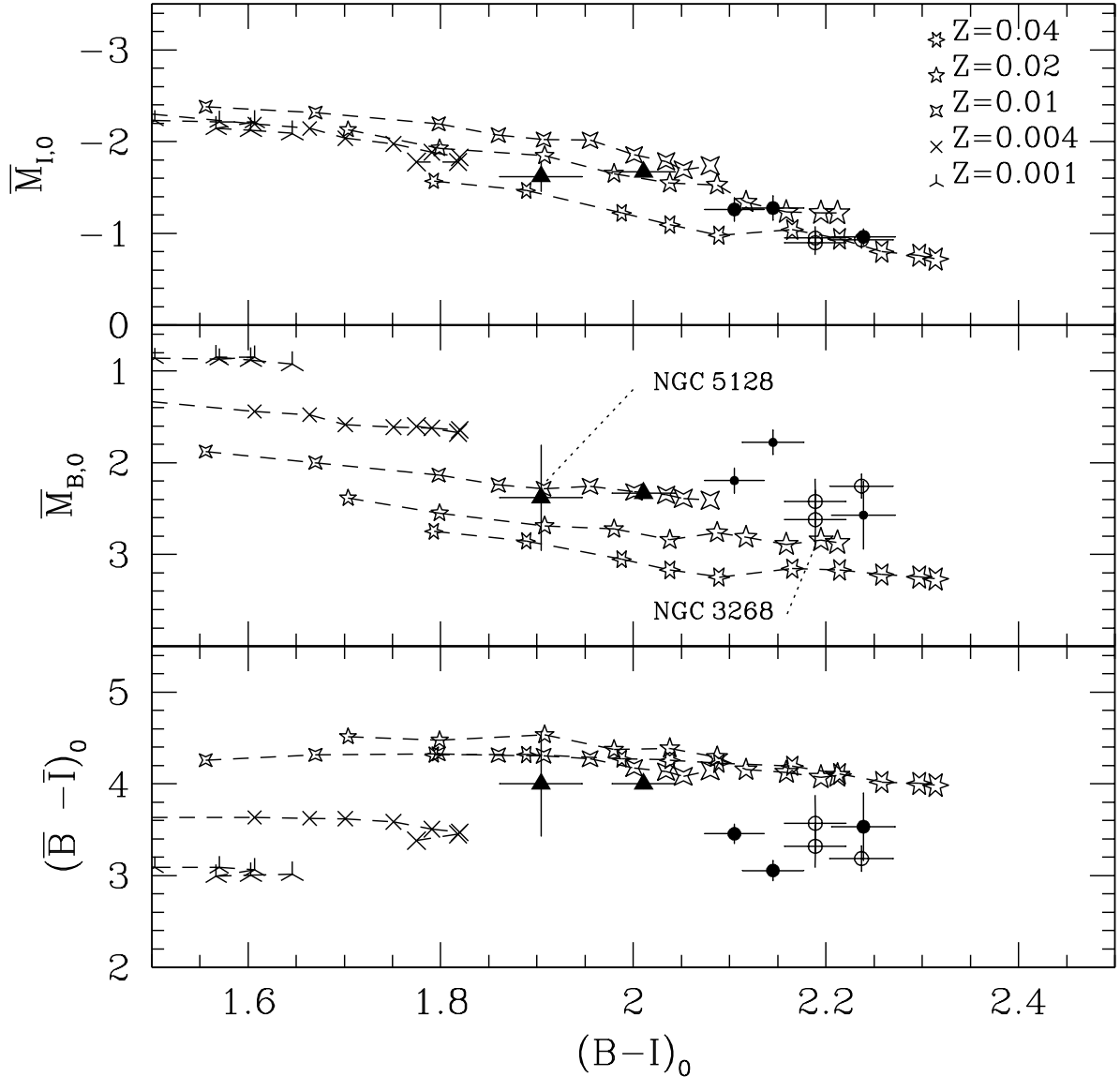


Fig. 4.— Observational data compared with models for various chemical compositions (upper right labels), with ages 1.5, 2, 3, 4, 5, 7, 9, 11, 13, and 14 Gyr (symbols with increasing size mark models of older age). Models are from SPoT web site (R05). Full (empty) circles mark the location of our ACS B-band reliable (unreliable) SBF measurements. Filled triangles show the location of M32 and NGC 5128. M32 and NGC 5128 $(B - I)_0$ error bars are evaluated taking into account the uncertainties of the $(B - I)_0$ -to- $(V - I)_0$ color transformation.

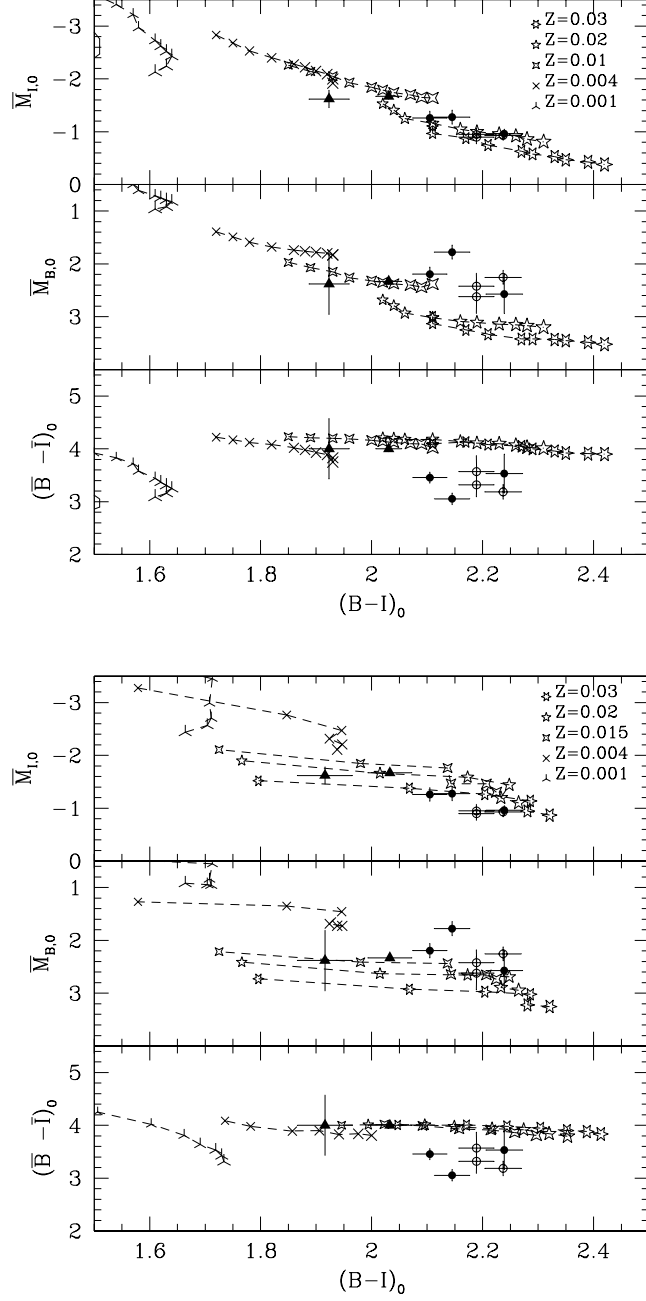


Fig. 5.— Same as Fig. 4 but for Blakeslee et al. (2001, upper panel), and Marín-Franch & Aparicio (2006, lower panel) models. The age of upper panel models ranges from 4 to 18 Gyr, with an increasing step of $\sim 12\%$. The ages for lower panel models are 3, 5, 7, 9, 11 and 13 Gyr (stellar tracks from Bertelli et al. 1994). Chemical compositions symbols are labeled upper right in the panels for both set of models.

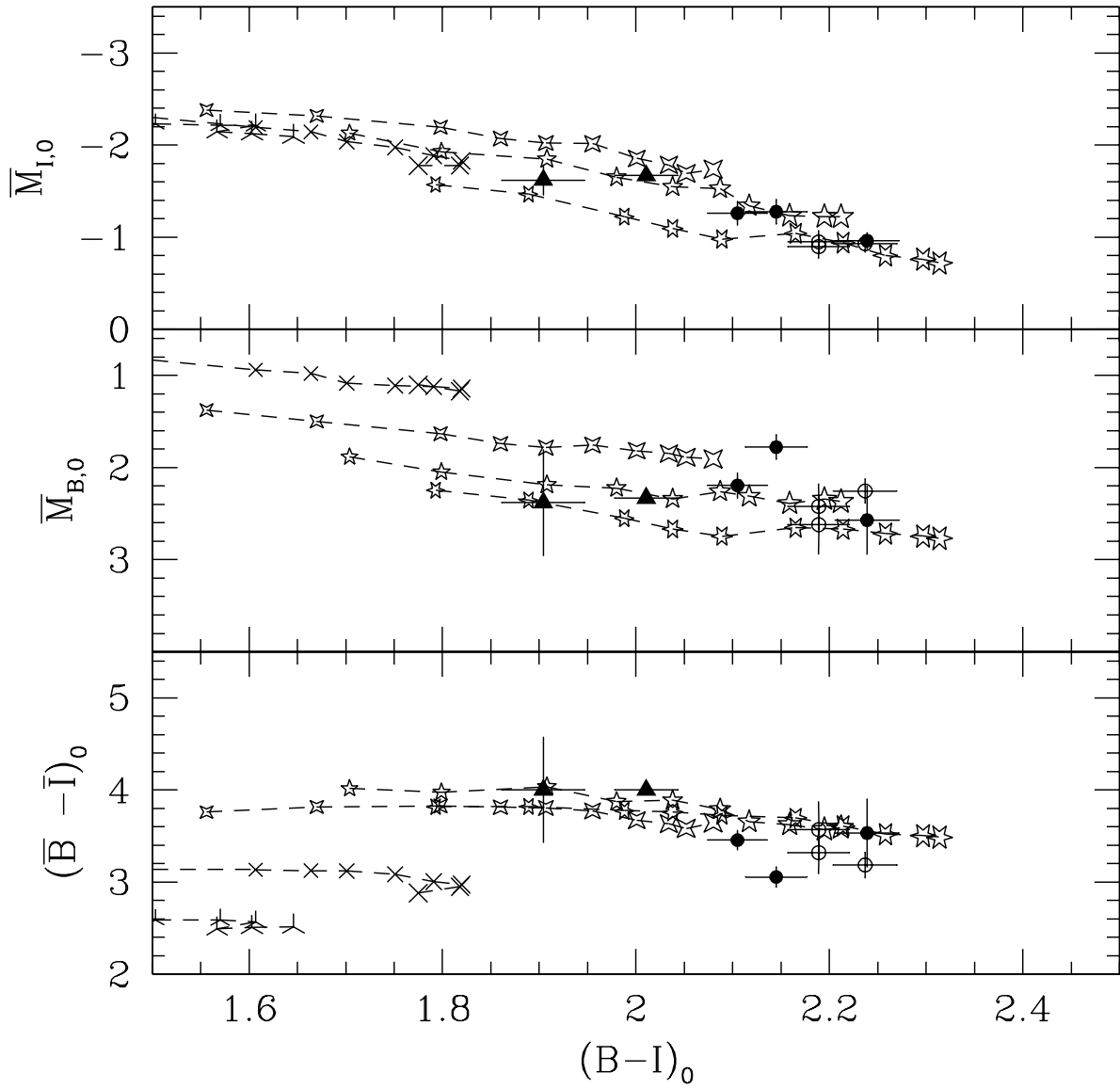


Fig. 6.— Same as Fig. 4 but models with an increased $N_{Post-AGB}/N_{HB}$ ratio (see text) are plotted.

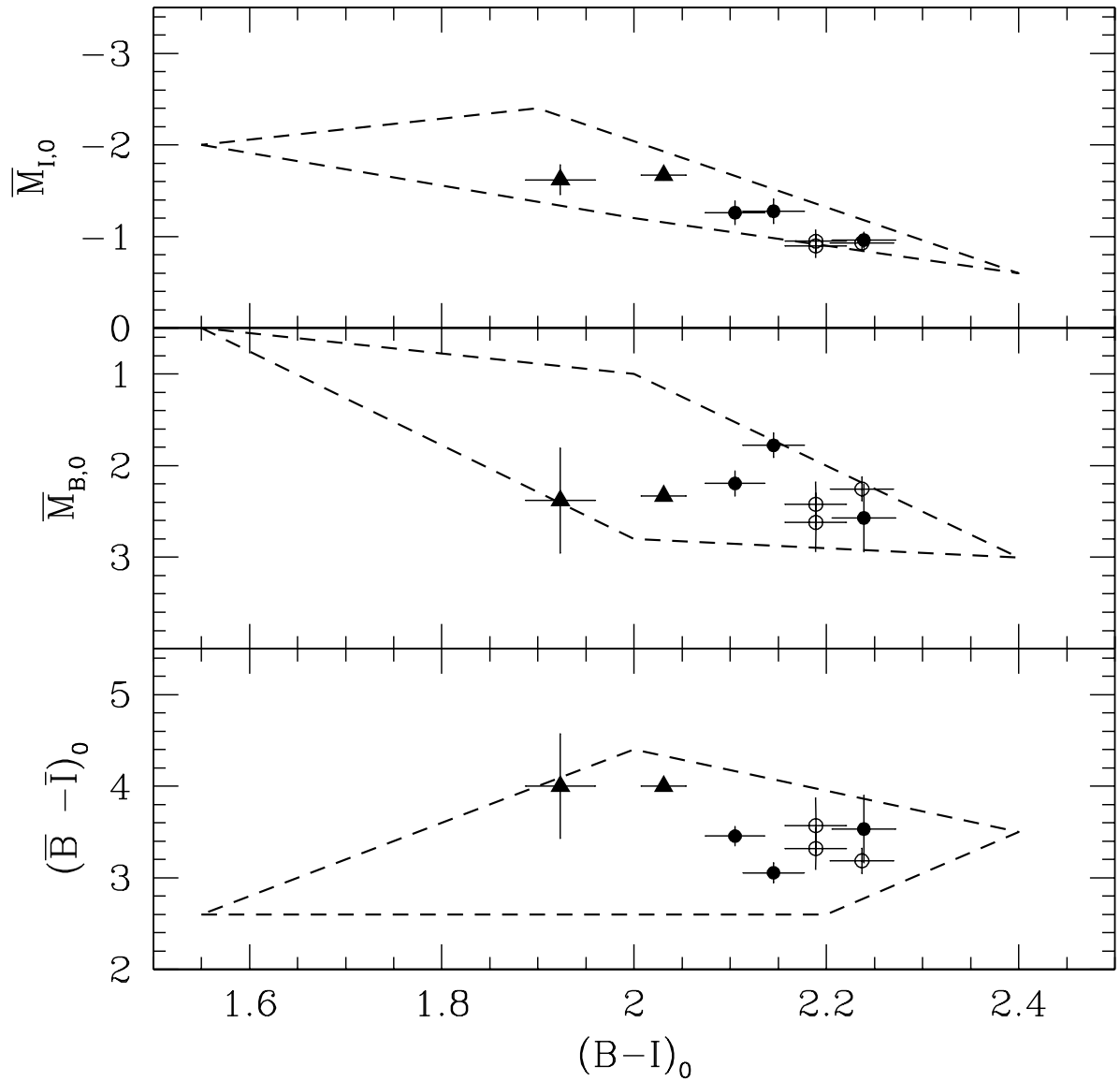


Fig. 7.— SBF data are compared with CSP models from BVA01. Symbols for observational data are as in Figure 4. For sake of clearness, only the edges of the CSP locations are shown.

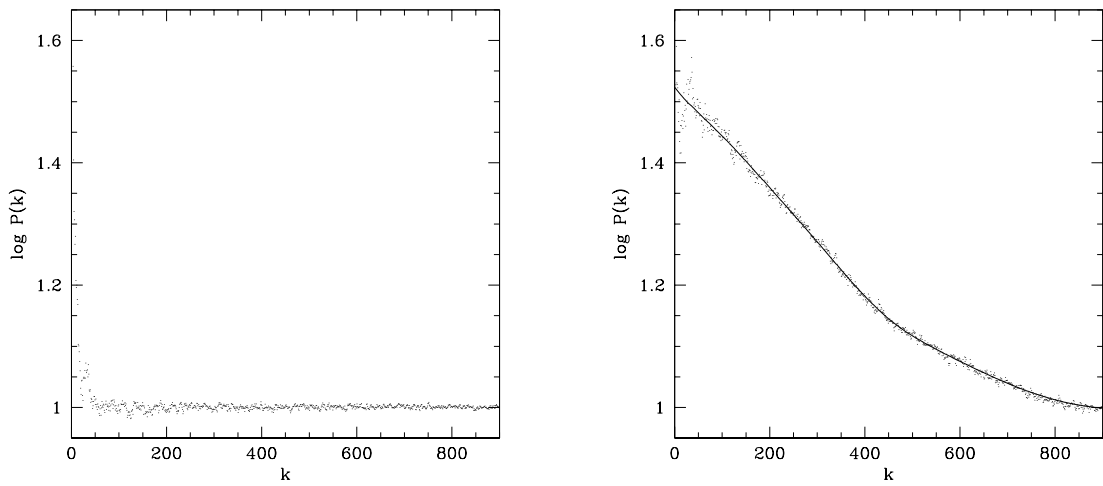


Fig. 8.— Power spectra of the residual frame for galaxy simulated without (left panel) and with (right panel) the SBF pixel-to-pixel variation. The strong variations visible at $k \leq 50$ are due to the extra correlation at these scales added by the large scale smoothing operation. In the right panel, the best fit to the data is shown as a solid line.